Turbulence measurements from velocimeters on compliant mid-water moorings, part 2: motion correction

LEVI KILCHER*, JIM THOMSON, SAMUEL HARDING AND SVEN NYLUND

ABSTRACT

THE ABSTRACT.

1. Introduction

Acoustic Doppler velocimeters (ADVs) have been used to make high-precision measurements of water velocity for over 20 years (Kraus et al. 1994; Lohrmann et al. 1995). During that time they have been deployed around the world to measure turbulence from a range of platforms, including: stationary structures on ocean- and lakebottoms, in surface waters from a pole lowered from a ship's bow, and in the deep ocean from autonomous underwater vehicles (e.g. Voulgaris and Trowbridge 1998; Zhang et al. 2001; Kim et al. 2000; Goodman et al. 2006; Lorke 2007; Geyer et al. 2008; Cartwright et al. 2009).

A relatively small fraction of ADV measurements have been made from moorings (e.g. Fer and Paskyabi 2014). Presumably this is because mooring motion can contaminate ADV measurements, and acoustic Doppler *profilers* (ADPs) can be used to measure mid-depth turbulence statistics without a mooring (e.g. Stacey et al. 1999a; Rippeth et al. 2002; Wiles et al. 2006). Still, ADV measurements have distinct characteristics that can be advantageous: they are capable of higher sample-rates, they have higher signal-to-noise ratios, and they have a much smaller sample-volume (1 centimeter, as opposed to several meters). That is, the ADV is a high precision instrument compared to an ADP, and it is therefore useful to have a method for making moored ADV measurements that account for mooring motion.

Inertial motion sensors (IMUs) have been used in the aerospace and aeronautical industries to quantify the motion of a wide range of systems—including aircraft, rockets, and spacecraft—for several decades, but their cost has come down as their market has grown beyond these niche sectors (Bevly 2004). Over the last ten years massive growth in the smart-phone, drone, and 'Internet of Things' markets has driven innovation in micro-electrical-mechanical systems (MEMS). One component that has emerged from this sector is the inertial motion unit (IMU), also known as the 'Magnetic, angular-rate, gravity' (MARG), or 'attitude heading reference system' (AHRS) sensor. These sensors measure three axes of: the earth's magnetic field, angular rotation, and linear acceleration. These signals are then integrated using Kalman filters to estimate the orientation and motion of the sensor (Barshan and Durrant-Whyte 1995; oáo Luis Marins et al. 2001; Bachmann et al. 2003)[1].

Nortek now offers a version of their Vector ADV with a Microstrain 3DM-GX3-25 IMU sensor (Nortek 2005; MicroStrain 2012). Nortek incorporated this IMU sensor's signals into the Vector data stream so that the motion and orientation signals were tightly synchronized with the ADV's velocity measurements. This tight synchronization provides a data-stream that can be utilized to quantify ADV motion in the earth's inertial reference frame, and remove that motion from the ADV's velocity measurements at each time-step of the its sampling. This work provides a detailed accounting for performing motion correction of these 'ADV-IMU' measurements, and presents results of this method using data from a range of mooring configurations that positioned ADV-IMUs at mid-depths in Puget Sound.

This effort was originally motivated by a need for low-cost, high-precision turbulence measurements for the emerging tidal energy industry (McCaffrey et al. 2015; Alexander and Hamlington 2015). Experience in the wind energy industry has shown that wind turbine lifetime is reduced by atmospheric turbulence, and the same is expected to be true for tidal energy turbines. In wind, meteorological towers are often used to position sonic anemometers at the hub-height of wind turbines for measuring detailed turbulence inflow statistics (Hand et al.

Corresponding author address: National Renewable Energy Laboratory, Golden, Colorado
E-mail: Levi.Kilcher@nrel.gov

---

[1] Within this literature, 'IMU' is generally reserved for a MARG sensor without a magnetometer, but herein we refer to the entire group of sensors that measure motion using accelerometers and angular-rate sensors as 'IMUs'.

2003; Kelley et al. 2005; Mücke et al. 2011; Afgan et al. 2013). In the ocean, tower-mounted hub-height turbulence measurements have been made, but they are challenging to install and maintain in energetic tidal sites (Gunawan et al. 2014). Thus, the Department of Energy funded this work to investigate the accuracy of mooring deployed ADV-IMUs to reduce the cost of turbulence measurements at tidal energy sites (Kilcher et al. 2016). The approach proved to be successful and potentially useful to the broader oceanographic community interested in moored turbulence measurements (Lueck and Huang 1999; Doherty et al. 1999; Nash et al. 2004; Moum and Nash 2009; Alford 2010; Paskyabi and Fer 2013).

The next section describes details of the measurements, including a summary of the hardware configurations (platforms) that were used to support and position the ADV-IMUs in the water-column. A detailed description of the motion of these platforms is found in the companion paper to this work, Harding et al. (2017), hereafter 'Part 1'. Section 3 describes the mathematical details of motion correction, and section 4 presents results from application of the method to measurements from the various platforms. Section 5 is a discussion of the energetics of the tidal channel where the measurements were made and demonstrates that the measurements are consistent with turbulence theory and other measurement in similar regimes. A summary and concluding remarks is found in section 6.

2. Measurements

This work is focused on measuring turbulence from ADVs that are deployed from non-stationary platforms and equipped with inertial motion sensors (IMU). The ADVs utilized for these measurements were all equipped with Microstrain 3DM-GX3-25 IMU sensors that captured all 6 components of the ADV motion (3 components of angular rotation and 3 components of linear acceleration), as well the orientation of the ADV pressure-case. The sampling of the motion sensor is tightly synchronized with the ADV measurements. The IMU measures its motion at 1kHz and uses internal signal integration (Kalman filtering) to output the motion signals at the same sample rate as the ADV's velocity measurements. This reduces aliasing of the IMU's motion measurements above the ADV's sample-rate (MicroStrain 2010). Cable-head ADVs were utilized throughout this work to allow for flexibility in the positioning of the ADV head relative to its pressure case.

All measurements used in this work were made in Admiralty Inlet, Washington, approximately 500 meters (m) WSW of Admiralty Head–Fort Casey State Park–in 60 m of water depth at latitude 48.153 north and longitude 122.687 west (Figure 1). The site is approximately 6 kilometers (km) east of Port Townsend, and 1 km north of the Port Townsend – Coupeville ferry route. Admiralty inlet is the largest waterway connecting Puget Sound to the Strait
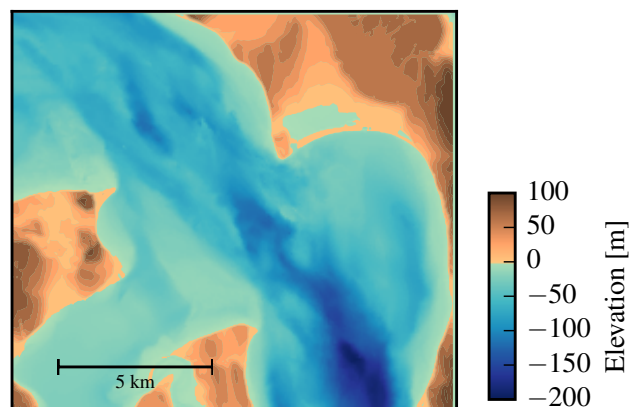

FIG. 1. Bathymetry of Admiralty Inlet at Admiralty Head.

of Juan de Fuca, and it possesses a large semi-diurnal tidal flow. This work utilizes data from three distinct deployment platforms: the 'tidal turbulence mooring', a 'Stable-Moor' buoy, and a simple sounding weight. Additional details, photos, and schematic diagrams of all three mooring systems can be found in Part 1.

a. Tidal Turbulence Mooring (TTM)

The 'tidal turbulence mooring' (TTM) is a simple mooring system with a 'strongback fin' suspended between a steel clump-weight anchor weighing 1200 kilograms (kg) when dry and a 0.93 m-diameter spherical steel buoy with a buoyancy of 320 kg. The ADV pressure cases were clamped to one side of the strongback fin and the ADV sensor head was positioned 10 cm in front of the fin's leading edge (Figure 2). The leading edge of the fin is fastened inline with the mooring line. This configuration was designed to work similar to a weather-vane, such that the drag on the fin held the ADV head upstream of the mooring components. This work utilizes data from two TTM deployments.

1) JUNE 2012 TTM DEPLOYMENT

The first was in June of 2012 at 48.15285 north, 122.68581 west. The mooring was in the water from 17:30 on the 12th until 14:30 on the 14th (local, i.e. pacific daylight time). Two Nortek ADVs were clamped to either side of the fin such that the axis of their cylindrical pressure-cases were parallel with the leading edge of the strongback. The ADV heads were spaced 0.5 m apart vertically along the fin. Only one of these ADVs was equipped with an integrated IMU. This TTM also had an upward-looking acoustic Doppler profiler mounted on the mooring anchor.

Periods of time during which this mooring interfered with a beam of the Doppler profiler were identified by inspection of the profiler's acoustic amplitude signal. Periods during which one beam of the profiler had $> 5\%$
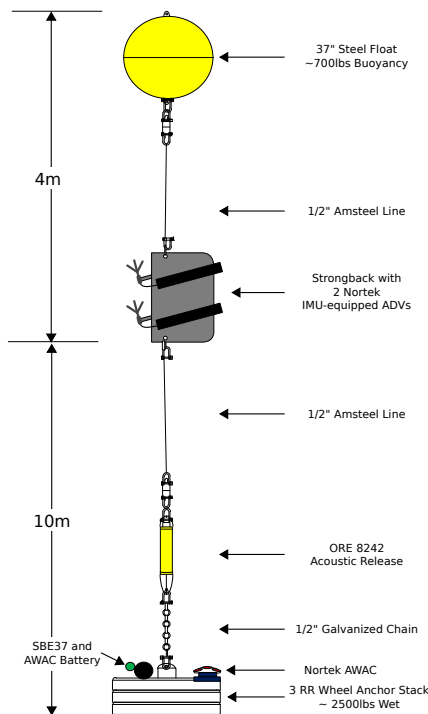
FIG. 2. Schematic diagram of the TTM, not to scale.

FIG. 3. TTM components on the deck of the R/V Jack Robertson. The TTM includes two ADVs, with pressure-cases mounted on opposite sides of the fin. The anchor stack includes a pop-up buoy for retrieval. The green arrow indicates the vector from the IMU to the ADV head (face of the transmit transducer).

higher acoustic amplitude than the other beams were flagged as 'contaminated' and excluded from averaging. 5-minute averages in which more than 50% of the data was contaminated in this way were masked as invalid.

2) JUNE 2014 TTM DEPLOYMENT

The second TTM deployment was in 2014 from 06:00 on June 17 to 05:00 on June 19 (local time). The mooring was positioned at 48.15327 north, 122.68654 west. Two Nortek ADV-IMUs were mounted on this TTM, with their heads spaced 0.5 m apart along the fin. In this case the pressure-cases and ADV heads were inclined at an angle of 18° to the leading edge of the fin to account for mooring blow-down during strong currents (Figure 3). This change was made to reduce vibrational motion observed during the June 2012 deployment that was believed to be associated with the orientation of the pressure cases.

b. The StableMoor platform

The second deployment platform was a cylindrical, 'StableMoor', syntactic foam buoy (manufacturer: Deep Water Buoyancy) that was anchored to a clump weight that weighed 2700 lbs (Figure 4). The buoy is 3.5 m long and 0.45 m in diameter with a tail ring that is 0.76 m in diameter. The StableMoor weighs 295 kg in air, and has a buoyancy of 185 kg in water.

The StableMoor was ballasted to pitch upward a few degrees in zero-flow to avoid 'flying downward'. In the presence of an oncoming current the tail fins help to orient it into the flow. The anchor for this buoy is similar to that of the TTM, including an acoustic release so the mooring and anchor can be recovered separately.

The StableMoor platform has two primary advantages compared to the TTM. First, it is significantly more massive and hydro-dynamically stable than the TTM, which reduces the frequency of motions of the platform. The other major advantage of the StableMoor platform is that it is capable of supporting a bottom-tracking acoustic Doppler profiler, which provides an independent measure of the platform's translational motion. Disadvantages of the StableMoor include: a) its size adds to the challenge of deployment and recovery, and b) it is significantly more expensive than the TTM system.

This work uses data from two deployments of the StableMoor. During both deployments the buoy was equipped with a 1200 kHz RDI workhorse sentinel acoustic Doppler profiler that was oriented downward-looking to measure water velocity below the platform in 12 1-meter bins and measure buoy motion ('bottom tracking'), all at a 1 Hz sample rate.

1) 'NOSE MODE' STABLEMOOR DEPLOYMENT

The StableMoor was deployed with an ADV-IMU mounted at its nose from 11:21 on May 12 to 11:53 on May 13, 2015 (local time). This deployment was at 48.15277 north, 122.68623 west. In this configuration the sample volume of the ADV, is 10 cm forward of the nose and 20 cm above the centerline of the StableMoor (Figure 4, middle), which is assumed to be outside of the bow wave of the StableMoor buoy (NEED CITATION for: any ideas on how big the bow wave of this sort of thing is?
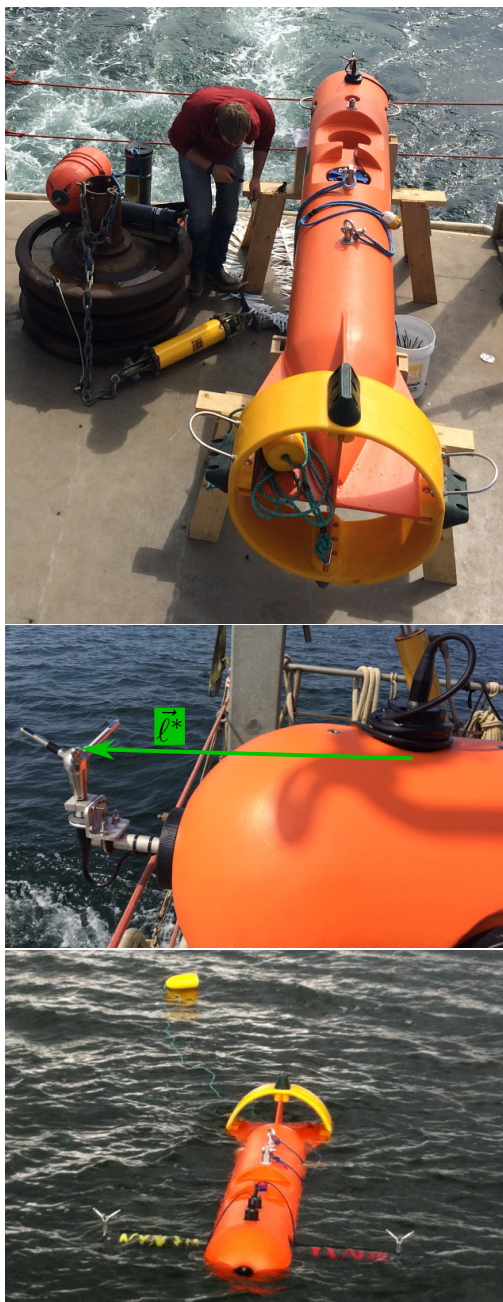
This configuration was designed to be the most stable platform for measuring turbulence from a moving platform.

2) 'WING MODE' STABLEMOOR DEPLOYMENT

The StableMoor buoy we used was customized to have an optional 1.5 m oval beam that holds two ADVs 0.53 m to either side of the buoy hull (Figure 4, bottom). The StableMoor was deployed in this configuration from 09:52 on May 11 to 06:23 on May 12, 2015 (local time). This configuration provides a simultaneous measurement of turbulence at two points laterally to the oncoming flow, which is a relatively unique mid-depth measurement.

c. Turbulence Torpedo

The turbulence torpedo is a simple sounding weight with an ADV head mounted forward of the nose, and the ADV pressure case strapped below. This platform was deployed on May 14, 2015 for 37 minutes starting at 07:41 local time. Position of deployment not mentioned in deck-log. Can we get this from ship data? Does this matter?. This measurement was made from a davit that hung the system from the side of the ship to a depth of approximately 25 m. The primary logistical advantages of this platform are its compact size, low cost, and the flexibility to perform spatial transects.

FIG. 5. The turbulence platform showing details of the ADV head and pressure case configuration. The green arrow indicates the vector from the IMU to the ADV head. The head-cable was taped out of the way beneath the sounding weight tail fins shortly after taking this photo.

FIG. 4. Top: Alex DeKlerk checks to ensure that the StableMoor buoy is properly fastened to its anchor; the RDI workhorse ADCP can be seen in the rear instrument bay. A bridle is draped across the top of the buoy for deployment and recovery, and a small marker buoy fastened to the tail is useful during recovery. Middle: a close-up of the StableMoor in the 'nose mode' configuration shows the ADV head and the top of its pressure case. The green arrow indicates the vector from the IMU to the ADV head. Bottom: the StableMoor buoy in 'wing mode', floating on the ocean surface with the marker buoy trailing behind. The ADV heads mounted at the ends of the cross-beam are protruding above the waterline.

d. Coordinate system and turbulence averaging

Unless stated otherwise, vector quantities in this work are in a fixed 'principal-axes' coordinate system that is aligned with the bi-directional tidal flow: positive u is in the direction of ebb (310° True), positive w is vertically upward, and v is the cross-stream component in a right-handed coordinate system. The full velocity vector, $\vec{\tilde{u}} = (\tilde{u}, \tilde{v}, \tilde{w})$, is separated into a mean and turbulent component as $\vec{\tilde{u}} = \vec{\bar{u}} + \vec{u}$, where the over-bar denotes a 5 minute average. Turbulence kinetic energy, tke $= \overline{u^2} + \overline{v^2} + \overline{w^2}$,

and Reynold's stresses, $\overline{uv}$, $\overline{uw}$, $\overline{vw}$ are computed by averaging over the 5-minute window. Throughout this work we use $\bar{U} = (\bar{u}^2 + \bar{v}^2)^{1/2}$ to denote the mean horizontal velocity magnitude.

All spectra, $S\{x\}(f) = |\mathscr{F}\{x(t)\}|^2$, and cross-spectra, $C\{x,y\}(f) = \text{real}(\mathscr{F}\{x(t)\}\mathscr{F}\{y(t)\})$, are computed using NumPy fast Fourier transform routines (van der Walt et al. 2011). Here, $\mathscr{F}\{x(t)\}$ denotes the fast Fourier transform of a signal $x(t)$. Time series', e.g. $x(t)$, are linearly detrended and Hanning windowed prior to computing $\mathscr{F}\{x\}$ to reduce spectral reddening.

Throughout the remainder of this work the dependence of S and C on f is implied (e.g. $S\{x\}(f)$ is hereafter $S\{x\}$), and for other variables the dependence on t is implied. Spectra and cross-spectra are normalized to preserve variance: $\int S\{u\}df = \overline{u^2}$, and $\int C\{u,v\}df = \overline{uv}$. The notations $S\{\vec{u}\} = (S\{u\}, S\{v\}, S\{w\})$ and $C\{\vec{u}\} = (C\{u,v\}, C\{u,w\}, C\{v,w\})$ denote the set of spectra and cross-spectra for each velocity component and pairs of components, respectively.

Turbulence dissipation rates are computed as,

$$\varepsilon = \frac{1}{\bar{U}} \left(\alpha \left\langle (S\{u\} + S\{v\} + S\{w\}) f^{5/3} \right\rangle_{fIS} \right)^{3/2} \quad (1)$$

Where $\alpha = 0.5$, and $\langle \rangle_{fIS}$ denotes an average over the inertial-subrange of the velocity spectra and where the signal-to-noise ratio is small (Lumley and Terray 1983; Sreenivasan 1995). Throughout this work we take this average from 0.3 to 1 Hz for the u and v components, and 0.3 to 3 Hz for the w component.

3. Methodology

REVISE THIS... An important detail of these methods is that the integration step tends to amplify small low-frequency bias-errors in the accelerometer and angular-rate measurements. The Kalman filtering utilizes the magnetometer measurements of the earth's magnetic field to provide an independent reference vector in the earth's coordinate system, and the accelerometer measurements of gravity provide a second reference vector. These vectors are used to stabilize orientation estimates in the earth's reference frame that would otherwise drift wildly due to the bias-errors (Haid and Breitenbach 2004; Madgwick et al. 2011). This approach is effective for stabilizing orientation estimates, but velocity estimates based on integration of the accelerometers is still subject to the low-frequency bias errors... These errors can be corrected by a stable estimate of velocity or position, or the velocity estimates derived from the IMU measurements must be interpreted with careful attention to the errors On the ocean surface,

GPS is increasingly being employed to provide is a frequently employed to low-frequency measurement of sensor motion or position is needed to... that would be contaminated by co correct for small biases in the angular stabilize the orientation estimates and correct for provide an independent estimate of stable estimate of the direction of the earth's magnetic field, are used to stabilize these errors by providing a low-frequencyso that the orientation measurements are stable and converge the provide the are utilized to... provide an independent is that These methods utilize the accelerometer signal to estimate the direction of the earth's gravity (i.e. down), and the magnetometer provides an estimate of the ,these methods utilize the rate sensors with the accelerometers and ... (Winkel et al. 1996) has one of the first 'multi-scale profilers' that quantified platform motion to estimate total velocity profile. (Stahr and Sanford 1999) used electromagnetic velocity measurements, with an ADCP that tracked the bottom to estimate the 'mean offset'. (Hayes et al. 1984) also used EM measurements(??), with calculations for body orientation changes. Miller et al. (2008) performed motion-correction of sonic anemometer data.

The essential approach of this methodology is to estimate time-series of velocity on a compliant mooring by obtaining an independent estimate of ADV head motion and removing that motion from the measured signal. Nortek offers an ADV that is equipped with an IMU that measures the linear acceleration, $\vec{a}$, rotational-motion, $\vec{\omega}$, and orientation matrix, $\mathbf{R}$, of the ADV pressure case (body) in the earth reference frame. So long as the ADV head is rigidly connected to the ADV pressure case, it is possible to utilize the IMU motion signals to calculate the motion of the ADV head, and remove it from the measured velocity signal. The ADV head motion, is calculated as the sum of rotational and translational motion:

$$\begin{aligned} \vec{u}_h &= \vec{u}_\omega + \vec{u}_a + \vec{u}_{low} \\ &= \mathbf{R}^T \cdot \vec{\omega}^*(t) \times \vec{\ell}^* + \int \{\vec{a}(t)\}_{HP(f_a)} dt + \vec{u}_{low} \end{aligned} \quad (2)$$

Here '$*$' superscripts denote quantities in the ADV's local coordinate system, and $\vec{\ell}^*$ is the vector from the IMU to the ADV head. $\mathbf{R}^T$—the inverse of the orientation matrix—rotates vectors from the IMU to the earth reference frame. The notation $\{\vec{a}\}_{HP(f_a)}$ indicates that the IMU's accelerometer signal is high-pass filtered (in the earth's stationary reference frame) at a chosen filter-frequency, f_a. This is necessary because accelerometers have low-frequency noise, sometimes referred to as 'bias-drift' (Barshan and Durrant-Whyte 1995; Bevly 2004; Gulmammadov 2009).

Integrating $\vec{a}$ to estimate $\vec{u}_a$ amplifies the bias-drift noise at low-frequencies, which dramatically reduces the signal-to-noise ratio at those time scales (Figure 3). The high-pass filtering reduces this noise so that it does not

contaminate motion correction, but real motion that exists at these frequencies is still lost in the low signal-to-noise ratio (Egeland 2014). This means that low-frequency motion is not well resolved by the IMU, and so there is a residual low-frequency translational motion, $\vec{u}_{\text{low}}$, that needs to be measured independently—or at the very least considered—when using motion corrected ADV-IMU data.

The choice of high-pass filter for low-frequency accelerometer noise depends on the flow conditions of the measurement, and the platform that is being used. In particular, filter-selection involves a trade off between filtering-out the bias-drift noise while not filtering-out measured motion that is unresolved by an independent measurement of $\vec{u}_{\text{low}}$. If an independent measure of low-frequency motion is available it can be used to increase the accuracy of $\vec{u}_{\text{h}}$ at low-frequency. Note that, to avoid double counting, $\vec{u}_{\text{low}}$ should be estimated by applying the complimentary low-pass filter to the independent measurement of low-frequency motion.

With this estimate of ADV head motion it is straightforward to correct the measured velocity, $\vec{u}_{\text{m}}$, to estimate the velocity in the earth's inertial reference frame:

$$\vec{u}(t) = \vec{u}_{\text{m}}(t) + \vec{u}_{\text{h}}(t) \qquad . \qquad (3)$$

Note here that the '+'-sign is correct because head motion, $\vec{u}_{\text{h}}$, induces a measured velocity in the opposite direction of the head motion itself ($\vec{u}_{\text{m}} = \vec{u} - \vec{u}_{\text{h}}$).

For the TTM and Turbulence Torpedo we utilize $f_a = 0.0333 Hz$ (30 second period), and assume that $\vec{u}_{\text{low}} = 0$. For the StableMoor $f_a = 0.2 Hz$ (5 second period). The bottom-track velocity was low-pass filtered at this frequency to provide an estimate of $\vec{u}_{\text{low}}$, and $\vec{a}$ was high-pass filtered at this frequency. We use 4-pole, bi-directional (zero-phase), Hanning filters for all filtering operations.

Additional details on motion correction–including a detailed accounting of the distinct coordinate systems of the IMU, ADV pressure case, and ADV head–can be found in Kilcher et al. (2016). Open-source Python tools for performing motion correction of ADV-IMU data–including scripts that write processed data in Matlab and tabulated formats–are available at `http://lkilcher.github.io/dolfyn/`.

4. Results

a. Mean velocity

Figure 7 shows a comparison of $\vec{u}$ measured by an ADV-IMU mounted on a TTM, to that of an upward-looking acoustic Doppler profiler mounted on the TTM anchor. This shows excellent agreement between the ADV and Doppler profiler measurements of velocity. The $\bar{u}$, $\bar{v}$ and $\bar{w}$ components have a root-mean-square error of 0.05, 0.13 and 0.03 m/s, respectively. While it is important to note
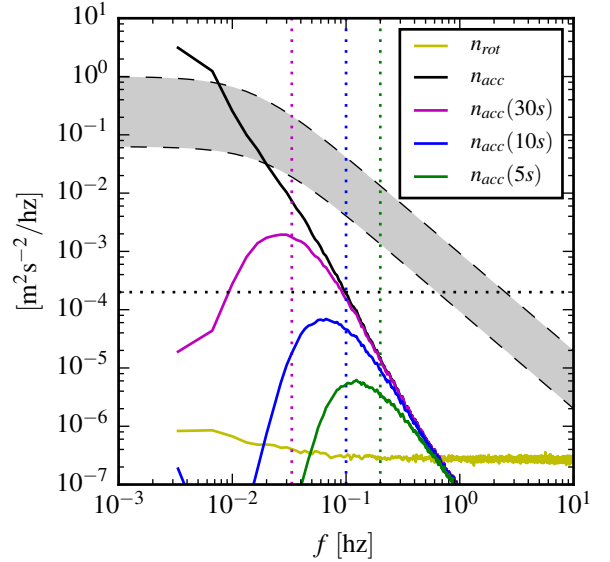

FIG. 6. Spectra of $\vec{u}_{\omega}$ (yellow) and $\vec{u}_a$ signals from the Microstrain IMU sitting on a motionless table. The $\vec{u}_a$ signals are unfiltered (black), and high-pass filtered at 30s (magenta), 10s (blue), 5s (green). Vertical dotted lines indicate the filter frequency. The black horizontal dotted line indicates the noise-level of a Nortek Vector ADV configured to measure ±4m/s. The shaded region indicates the range of spectra presented herein ($0.002 < \text{tke} < 0.03 \text{ m}^2/\text{s}^2$, 1e-5 $< \varepsilon <$ 5e-4 W/kg).

that their is some discrepancy between ADP and ADV measured velocities (especially in $\bar{v}$, which is most likely due to incomplete motion correction), the agreement between the magnitude and direction of these independent velocity measurements indicates that moored ADV-IMUs provide a reliable estimate of velocity in the Earth's reference frame.

b. TTM spectra

As discussed in detail in Part 1 the mooring motion of the TTM, $S\{\vec{u}_{\text{h}}\}$, has a peak at 0.1 to 0.2 Hz from swaying of the mooring that is most likely driven by eddy-shedding from the spherical buoy (Figure 8, red lines). There is also higher-frequency broad-band motion that is associated with fluttering of the strongback fin around the mooring line. Both of these motions are especially energetic in the v-component spectra, because this is the direction in which the TTM mooring system is most unstable. As is expected from fluid-structure interaction theory the amplitude of these motions increases with increasing mean velocity (Morison et al. 1950). Should we move this sentence and reference to Part 1, or leave it in here?

The mooring motion contaminates the uncorrected ADV-measurements of velocity, $S\{\vec{u}_{\text{m}}\}$, whenever the amplitude of the motion is similar to or greater than the amplitude of the turbulence. Fortunately, much of this motion can be removed using the IMU's motion signals as detailed
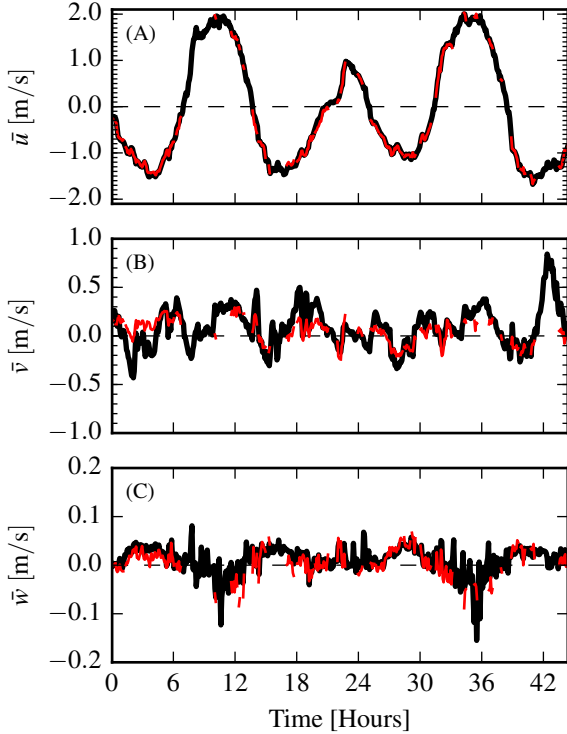
FIG. 7. Time series of tidal velocity at Admiralty Head from TTM measurements (black), and an acoustic Doppler profiler (red). The profiler measurements–taken at the same depth as the ADV on the TTM— were contaminated by acoustic reflection from the strongback fin when it was inline with one of the profiler's beams. Note that the vertical scale on the three axes vary by more than an order of magnitude; the small ticks in A and B are equivalent to the ticks in C.

in section 3. Lacking an independent measurement of turbulence velocity at this site, we interpret the agreement of these spectra with turbulence theory as evidence of the success of the method. In particular, at high-frequencies ($f > 0.3$ Hz) for each mean-flow speed the spectra decay with a $f^{-5/3}$ slope and have equal amplitude across the velocity components. These results are consistent with Kolmogorov's (1941) theory of isotropic turbulence, and are consistent with other measurements of turbulence in energetic tidal channels from stationary platforms (Kolmogorov 1941; Walter et al. 2011; Thomson et al. 2012; McMillan et al. 2016).

At low frequencies, the spectra tend to become roughly constant (especially at higher flow speeds), which is also consistent with previous works. Note here, that the very-low magnitude of $S\{\vec{u}_h\}$ at low frequencies is partially a result of filtering the IMU's accelerometer signal when calculating $\vec{u}_a$. The true low-frequency spectrum of ADV-head motion is unknown (indicated using a dashed line below f_a). A comparison of $S\{\vec{u}\}$ measured by the TTM to that measured by the ADP—during the June 2012

deployment—are in agreement at low-frequencies (not shown). This suggests that the assumption that $\vec{u}_{low} = 0$ at these frequencies, at this site, for this platform is justified—even if $S\{\vec{u}_h\}$ is not as low as indicated in Figure 8.

As successful as motion correction is, some of the motion contamination persists in $S\{\vec{u}\}$. This is most notable in $S\{v\}$ at the highest flow speeds (> 2.0 m/s): a peak at 0.15 Hz is an order of magnitude larger than a spectral fit to the other frequencies would indicate. This persistent motion contamination is evident to a lesser degree in $S\{u\}$ for $|u| > 2$ m/s, and in $S\{v\}$ at lower flow speeds. $S\{w\}$ appears to have no persistent motion contamination because the amplitude of the motion in this direction is much lower than for the other two components. For these measurements, $S\{w_h\}$ is so low that w-component motion correction is only necessary when $|u| > 2$ m/s.

The amplitude of the persistent motion contamination peaks in $S\{v\}$ at 0.15 Hz are a factor of 5 to 10 times smaller than the amplitude of the ADV head motion itself. This suggests the Microstrain IMU can be used to effectively correct for mooring motion at 0.15 Hz when the amplitude of that motion is less than 3 times the amplitude of the real turbulence spectrum. Where we have chosen a value of 3 as a conservative estimate of motion correction's effectiveness.

This reveals an ancillary benefit of the IMU measurements: in addition to the primary benefit of correcting for mooring motion, they can also be used to identify and screen-out persistent motion contamination. For example, one of the most common uses of turbulence spectra is for the calculation of ε and tke. For these purposes, based on the relative amplitudes of the 0.15 Hz peaks, we assume that persistent motion contamination is likely where $S\{\vec{u}_h\}/S\{\vec{u}\} > 3$ and exclude these regions from spectral fits.

In the present case, for the u and w spectra, this criteria only excludes a narrow range of frequencies at the 0.15 Hz motion peak for some cases. This criteria is more restrictive of the v-component spectra at high frequencies for $\bar{U} > 1.0$ m/s, but this may be acceptable because the amplitude of the spectrum at these frequencies—i.e. in the isotropic inertial subrange—should be equal to that of u and w (Kolmogorov 1941).

Agreement of the v-component spectral amplitude with that of u and w at frequencies > 0.3 Hz indicates that motion correction is effective at those frequencies even when $S\{\vec{u}_h\}/S\{\vec{u}\} > 3$. This suggests that our screening threshold is excessively conservative at those frequencies, and that a more precise screening threshold is frequency dependent. For example, it might take into account the f^3 character of the noise in $S\{\vec{u}_a\}$ (Figure 3). For the purposes of this work the $S\{\vec{u}_h\}/S\{\vec{u}\} < 3$ threshold for spectral fits is sufficient, and detailed characterization of the
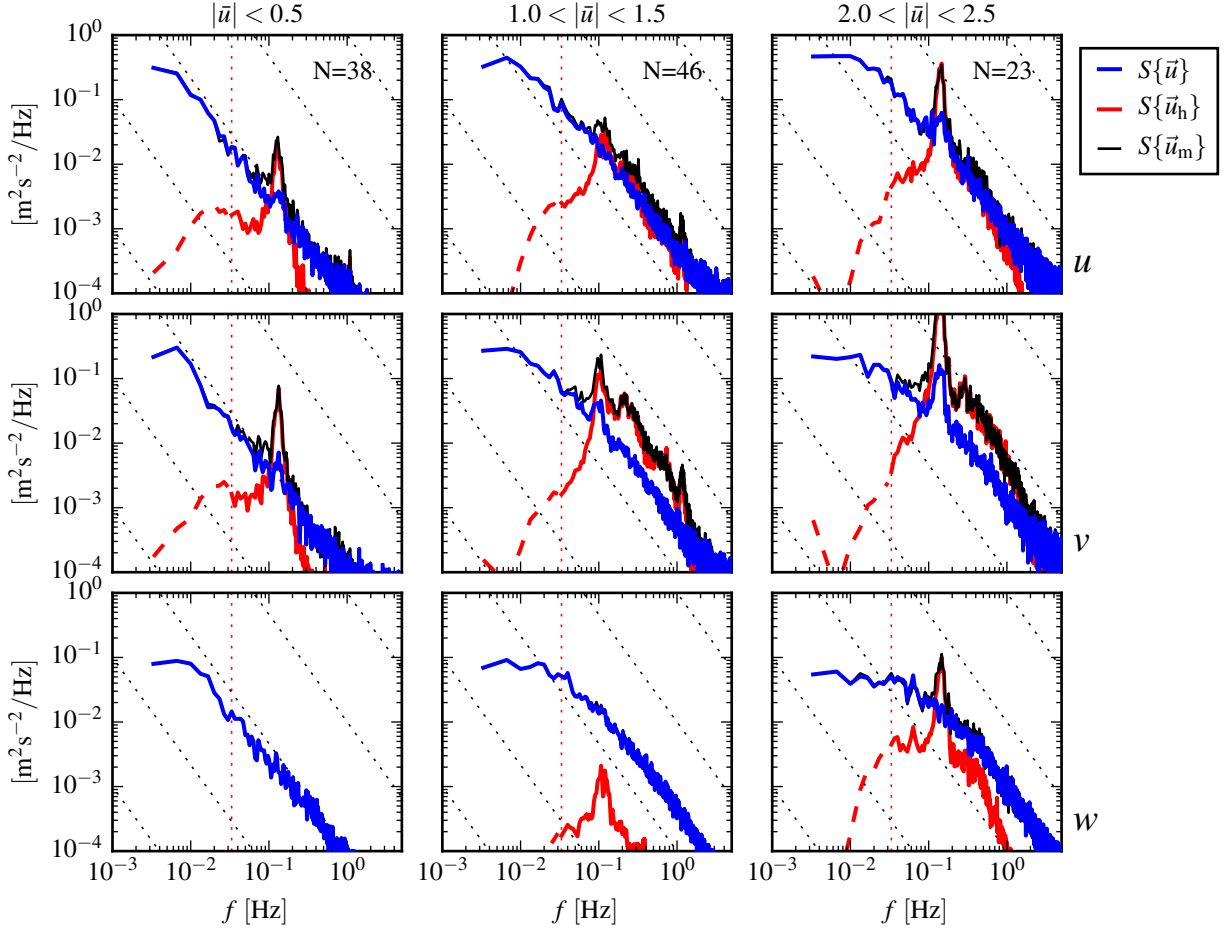
FIG. 8. Turbulence spectra from the June 2014 TTM deployment. Each column is for a range of streamwise velocity magnitudes (indicated at top). The rows are for each component of velocity (indicated to the lower-right of the right column). The uncorrected spectra are in black and the corrected spectra are blue, and the spectra of ADV head motion, $\vec{u}_h$, is red (also indicated in the legend). The vertical red dotted line indicates the filter frequency applied to the IMU accelerometers when estimating $\vec{u}_h$; below this frequency $S\{\vec{u}_h\}$ is plotted as a dashed line. Diagonal black dotted lines indicate a $f^{-5/3}$ slope. The number of spectral-ensembles, N, in each column is indicated in the top row.

IMU's motion- and frequency-dependent noise level is left for future work.

c. StableMoor Spectra

The spectra of the stablemoor motion has a broader peak with a maximum amplitude that is approximately half the frequency of the TTM spectral peak (Figure 9). The motion of this platform also does not have high-frequency 'sub-peaks' or other high-frequency broadbanded excitation (Part 1). Is the following in part 1: These characteristics of the motion are most-likely due to the more massive and hydro-dynamically streamlined properties of the platform.

Like the TTM, the motion-corrected spectra from the StableMoor are consistent with turbulence theory and previous observations. Most importantly, there is an improve-

ment in the quality of the motion corrected spectra compared to the TTM. In particular the persistent motion contamination peaks appear to be completely removed. That is, this measurement system provides an accurate estimate of the turbulence spectra at this location from low frequencies to more than 1Hz—well into the inertial sub-range—for all three components of velocity.

Note that this level of accuracy can not be obtained without the independent estimate of $\vec{u}_{low}$. If we assume that $\vec{u}_{low} = 0$ a similar plot to Figure 9 (not shown) reveals persistent motion-contamination peaks and troughs in the u- and v-spectra regardless of the choice of f_a. This indicates that the low-frequency motion of the StableMoor is below a threshold where the IMU's signal to noise ratio is high enough to resolve its motion. In other words, compared to the TTM, the StableMoor platform provides a
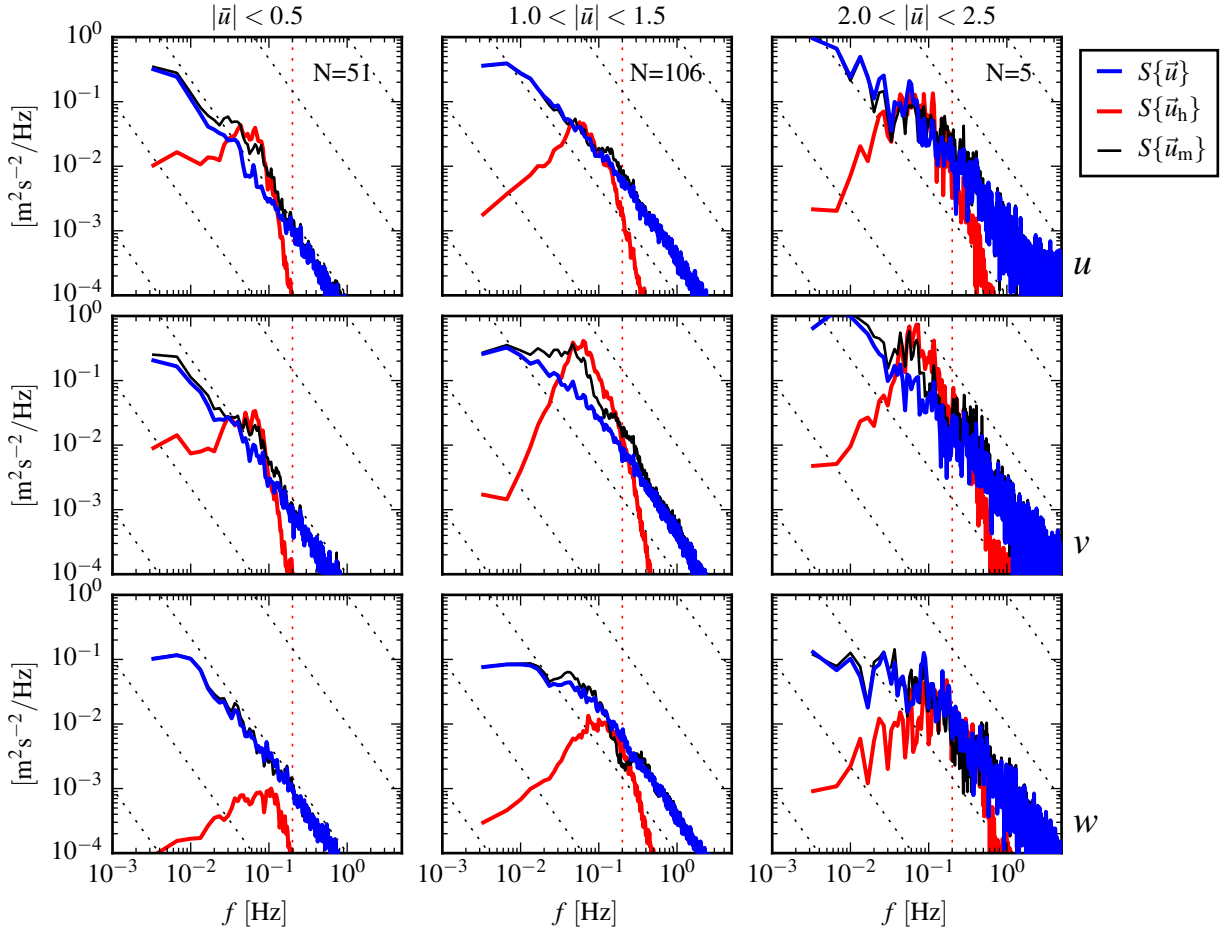
FIG. 9. Turbulence spectra from the StableMoor buoy. The axes-layout and annotations are identical to Figure 8, except that $S\{\vec{u}_{\mathrm{h}}\}$ is plotted as a solid line at all frequencies because it is measured at all frequencies.

more accurate measurement of turbulence when it includes an independent measure of $\vec{u}_{\mathrm{low}}$ (here a bottom-tracking ADCP), but it does no better—and perhaps worse—when it doesn't.

d. Torpedo spectra

The u and v motion of the turbulence 'torpedo' is broadbanded and the w motion has a narrow peak at 0.3 Hz (Figure 10). Because $\vec{u}_{\mathrm{h}}$ is estimated using $f_a = 0.0333Hz$ and assuming $\vec{u}_{\mathrm{low}} = 0$ its spectra rolls-off quickly below f_a. A better estimate of $\vec{u}_{\mathrm{low}}$ could be obtained by accounting for ship motion, but this has not been done here. ← Should we do this?

Motion correction of the torpedo data appears to effectively remove a motion from $S\{w\}$ at 0.3Hz, and straightens out $S\{v\}$ between 0.04 and 0.6Hz. $S\{u\}$ is relatively unimproved by motion correction, apparently because the torpedo motion is smaller than the turbulence in this direction. At frequencies below f_a, $S\{u\}$ and $S\{v\}$ increase

dramatically. This suggests that unresolved low-frequency motion of the torpedo is contaminating the velocity measurements at these frequencies. It may be possible to correct for some of this using a measurement of the ship's motion as a proxy for the torpedo's low-frequency motion, but this has not been done. Still, above f_a, the torpedo appears to provide a reliable estimate of spectral amplitude in the inertial subrange and can therefore be used to estimate ε. Considering the simplicity of the platform it may be a useful option for quantifying this essential turbulence quantity in a variety of scenarios. If a GPS is positioned above it, it may be capable of providing even more.

e. Cross-spectra

Inspection of cross-spectra from TTM measurements demonstrates that motion correction can reduce motion contamination to produce reliable estimates of velocity cross-spectra (Figure 11). At low flow speeds (left column), cross-spectra between components of $\vec{u}_{\mathrm{h}}$ (i.e. be-
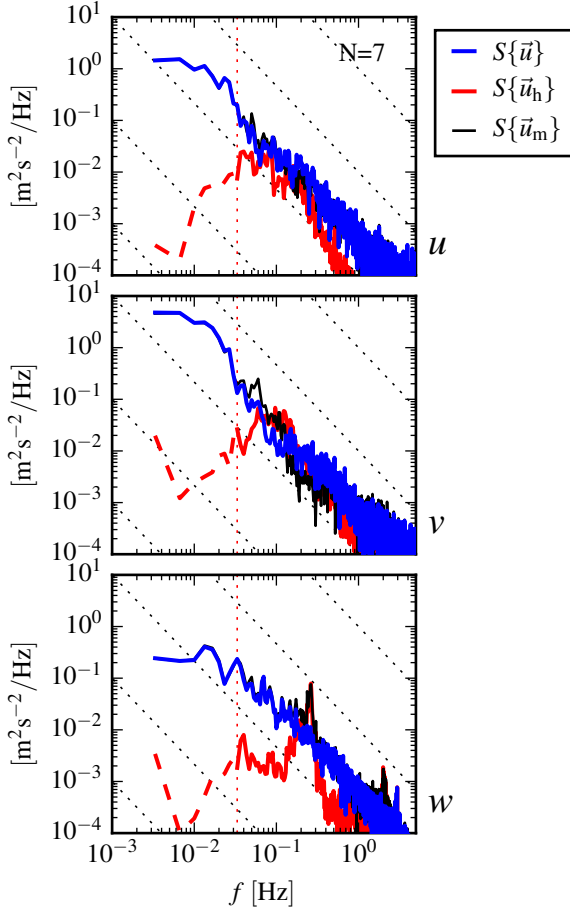
FIG. 10. Turbulence spectra from the turbulence torpedo during a 35 minute period when the mean velocity was 1.3 m/s. Annotations and line colors are identical to Figure 8.

tween components of head-motion, red) are small compared to correlated velocities. As the velocity magnitude increases (center, and right columns), the swaying motion of the TTM at 0.15 Hz appears as a peak in the amplitude of the cross-spectra of $\vec{u}_h$ and $\vec{u}_m$ (black) for all three components of cross-spectra (rows). Fortunately, motion correction reduces the amplitude of this peak dramatically so that $C\{\vec{u}\}$ (blue) is small at 0.15 Hz compared to lower frequencies. Furthermore, the fact that the standard deviation of $C\{\vec{u}\}$ is also relatively small at 0.15 Hz suggests that motion correction is effective for each spectral window, not just in their mean.

These results indicate that motion-corrected TTM velocity measurements can be used to obtain reliable estimates of turbulence Reynold's stresses, which are the integral of the cross-spectra. Without motion correction, Reynold's stress estimates would be contaminated by the

large peaks in the cross-spectra that are due to the swaying and fluttering motion of the TTM vane.

A similar investigation of StableMoor cross-spectra (not shown) indicates that cross-spectral motion contamination is much lower amplitude than for the TTM. The low-frequency (< 0.3 Hz) 'swimming' motion of that platform produces minimal cross-spectral signal, and the relative large-mass of the platform minimizes the kinds of higher-frequency swaying/fluttering that creates large values of cross-spectral head-motion. Thus, the StableMoor platform also produces reliable estimates of Reynold's stresses, which are presumed to be improved by motion correction.

5. Discussion

The beginning of the previous section presented a comparison of $\vec{u}$ measured by a TTM-mounted ADV, to measurements from a co-located ADP. This demonstrated that the IMU provides a reliable estimate of the ADV's orientation and that this can be utilized to estimate mean velocity in the earth's reference frame. Turbulence velocity estimates from the same ADP are also in agreement with low-frequency TTM turbulence estimates (not shown), but the ADP does not resolve turbulence at the scales where motion contamination is strongest (0.1 to 1.0 Hz).

Ideally, moored motion-corrected turbulence velocity measurements would be validated against simultaneous independent validated measurements of turbulence velocity at the same scales, exact time and exact location. Accomplishing this, however, involves significant technical challenges not easily overcome—most notably the difficulty of measuring turbulence at the same point as the moving ADV. A slightly less ideal but much more realistic confirmation of the methodology might involve comparing the statistics of moored turbulence measurements to that from a nearby fixed platform, or a fixed platform placed at the same location at a different time (e.g. the 'TTT' platform described in Thomson et al. 2012). Unfortunately, to our knowledge, these measurements have not yet been made.

Lacking a relevant, fixed, independent turbulence measurement to compare to it is instructive to demonstrate the degree to which the moored measurements are consistent with turbulence theory and other turbulence measurements in similar flow environments. The previous section showed that the shape of the turbulence velocity spectra from moored ADVs is consistent with Kolmogorov's theory of locally isotropic turbulence, which has been observed consistently in turbulence measurements for decades (Kolmogorov 1941; Grant et al. 1962; McMillan et al. 2016). In particular, we observed an isotropic subrange—an $f^{-5/3}$ spectral slope, and equal amplitude spectra between components—that is driven by anisotropic turbulence at longer time-scales (Figures 8, 9,
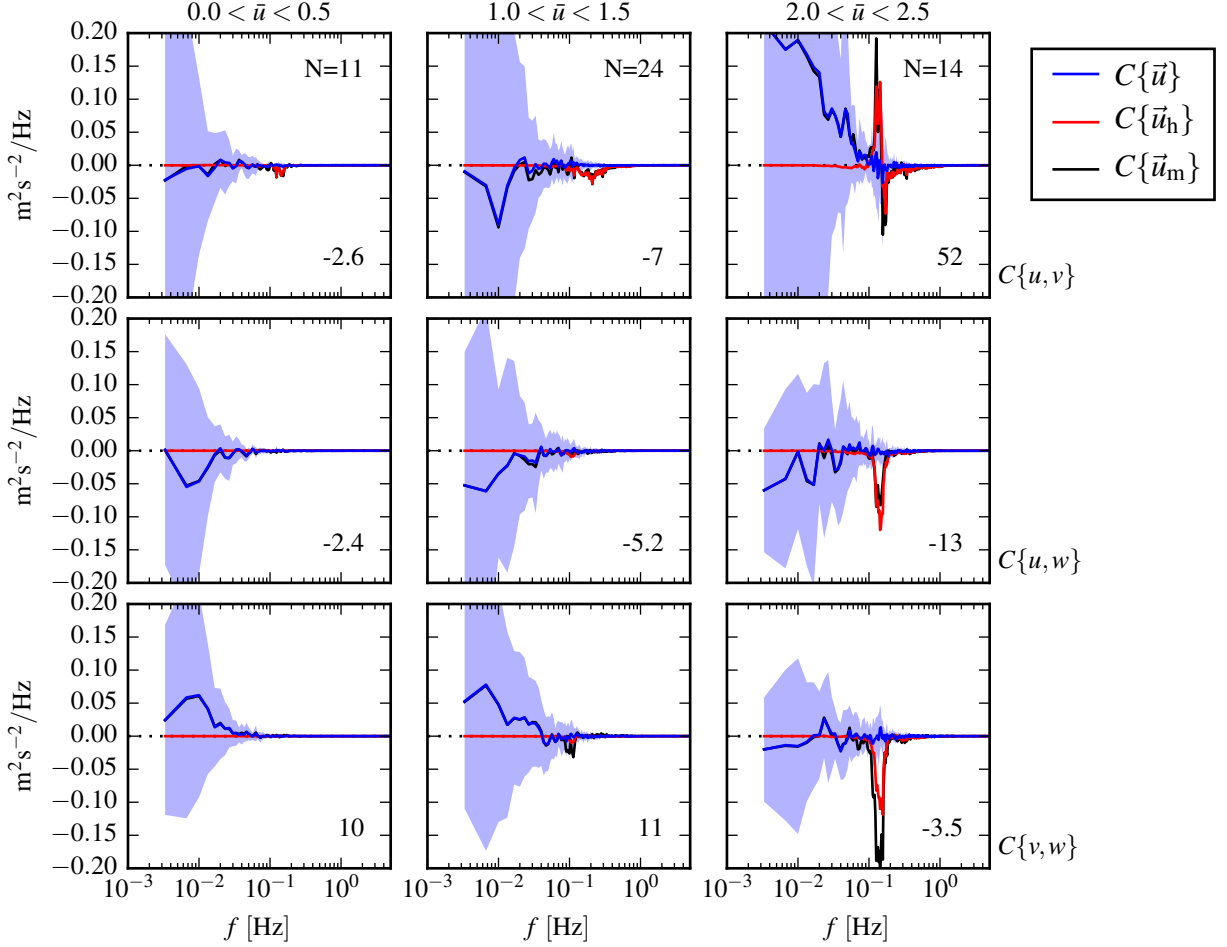
FIG. 11. The real part of the cross-spectral density between velocity components measured by the TTM. The upper-row is the *u-v* cross-spectral density, the middle-row is the *u-w* cross-spectral density, and the bottom-row is the *v-w* cross-spectral density. The columns are for different ranges of the stream-wise mean velocity magnitude (indicated above the top row). The blue line is the cross-spectrum between components of motion-corrected velocity, the red line is the cross-spectrum between components of head-motion, and the black line is the cross-spectrum between components of uncorrected velocity. The light-blue shading indicates one standard deviation of the C for the motion corrected cross-spectral density. N is the number of spectral ensembles in each column. The number in the lower right corner of each panel is the motion-corrected Reynold's stress (integral of the blue line) in units of 1e-4 $m^2 s^{-2}$.

10). This is interpreted as the first indication that the measurement systems presented are capable of accurately resolving turbulence. The degree to which uncorrected spectra were corrected toward this theoretical and observationally confirmed shape is interpreted as a measure of the improvement of the spectral estimates by motion correction.

Figure 12 presents a time-series of the mean velocity (A) and several turbulence statistics that were measured during the June 2014 TTM deployment. This figure shows the evolution of the flow through Admiralty Inlet during 1.5 tidal cycles. The tke (B), Reynold's stresses (C), dissipation and one component of turbulence production (D) grow and strengthen with ebb or flood, then subside during slack tide. This component of turbulence production

is:

$$P_{uz} = \frac{\partial \bar{u}}{\partial z} \overline{uw} \qquad . \qquad (4)$$

Where $\partial \bar{u}/\partial z$ is computed from the two ADV's on the TTM. The highest values of ε and P_{uz} occur at the peak of the ebb or flood, which is in agreement with other measurements in tidal channels. The agreement of the magnitude of P_{uz} with ε at those times suggests a local production-dissipation balance that is often observed in tidally forced channels (Trowbridge et al. 1999; Stacey et al. 1999b; McMillan et al. 2016). At other times the value of P_{uz} is insufficient to balance ε or is negative.

Inspection of the negative P_{uz} values reveals that most of them are due to a reversed sign of $\overline{uw}$ rather than a re-
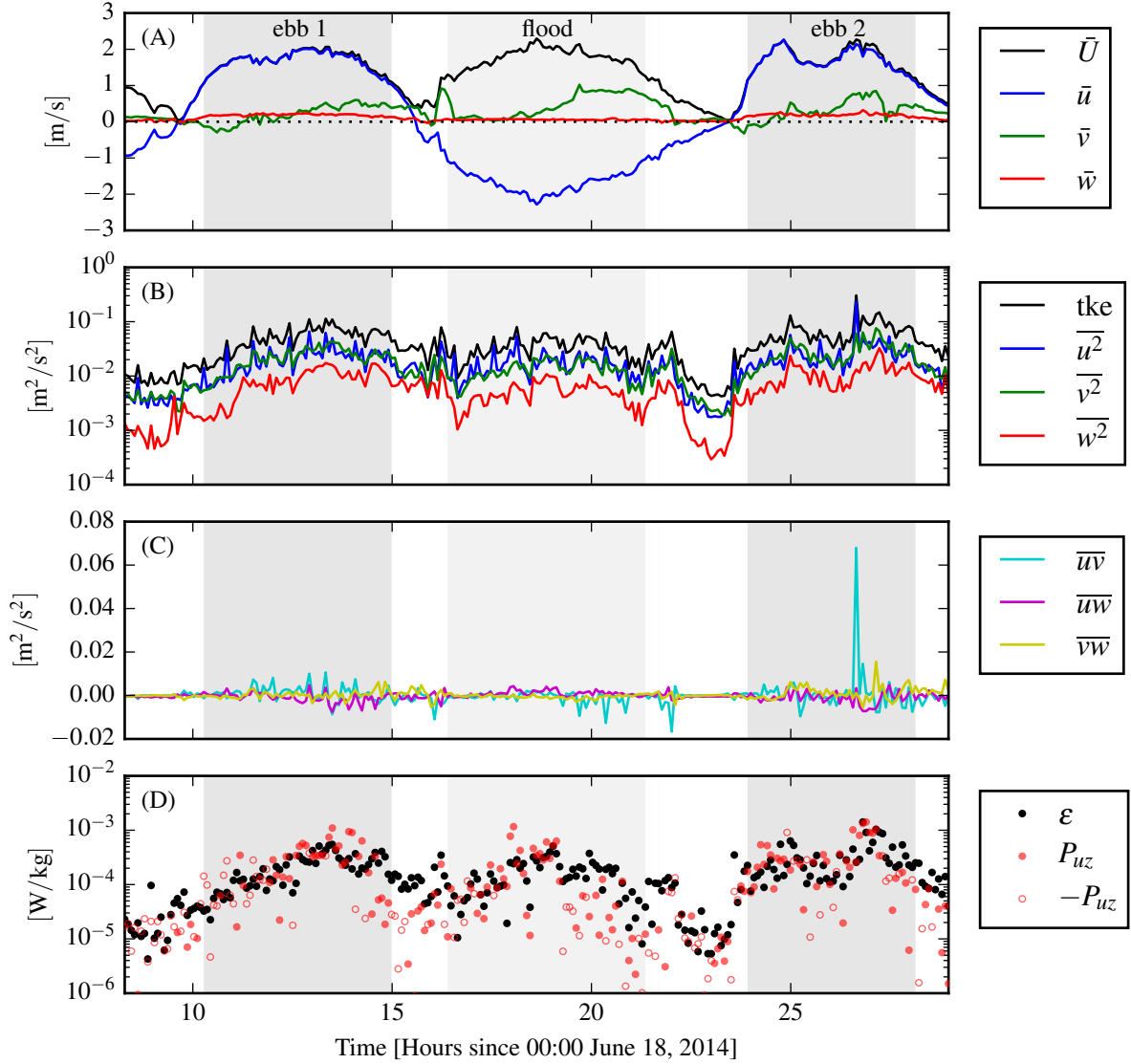
FIG. 12. Time-series of mean velocities (A), turbulence energy and its components (B), Reynold's stresses (C), and turbulence dissipation rate (D) measured by the TTM during the June, 2014 deployment. Shading indicates periods of ebb ($\bar{u} > 1.0$, grey), and flood ($\bar{u} < -1.0$, lighter grey).

versed sign of $\partial u/\partial z$ (i.e. when compared to the sign of u). This suggests that uncertainty in $\overline{uw}$ may be contributing to discrepancies between P_{uz} and ε. It is also possible that other terms of the tke equation are important, such as other components of production, advection terms, or turbulent transport terms.

Figure 13 compares individual values of P_{uz} with ε directly. Given the assumptions implicit in this comparison, and the discussion above, the agreement between P_{uz} and ε is an encouraging result that suggests the turbulent boundary reaches the depth of these measurements (10 m) during the highest flow speeds. This result is further supported by a comparison of $\bar{U}$ with ε (Figure 14). Here

we see a $\varepsilon \propto \bar{U}^3$ dependence that is again suggestive of bottom boundary layer physics (Trowbridge 1992; Nash et al. 2009). At lower flow speeds, ε deviates from this relationship, which suggests that the boundary layer is no longer the dominant physical process at the depth of these measurements.
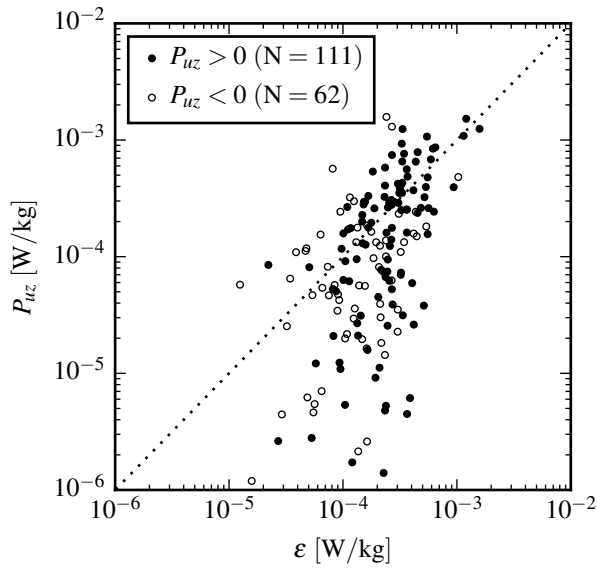
6. Conclusion

FIG. 13. P_{uz} vs. ε during the June 2014 TTM deployment for values of $|u| > 1$ m/s. Values of 'negative' production are indicated as open circles.
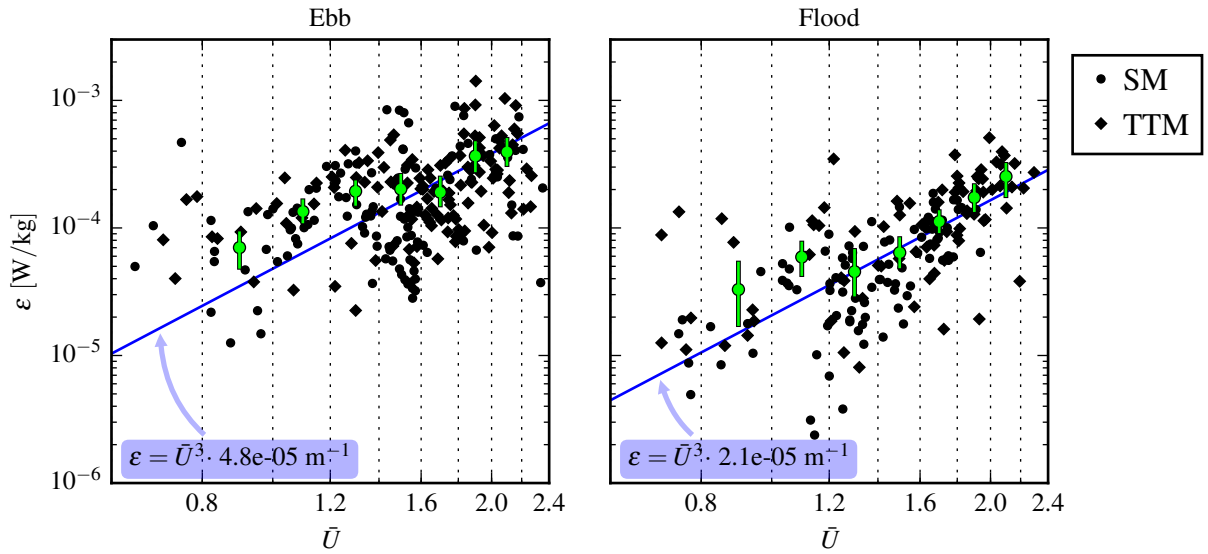
FIG. 14. A log-log plot of ε versus $\bar{U}$ for the June 2014 TTM (diamonds) and May 2015 StableMoor (dots) deployments, during ebb (left) and flood (right). Black points are 5 minute averages. Green dots are mean values within speed bins of 0.2 m s^{-1} width that have at least 10 points (50 minutes of data); their vertical bars are 95% bootstrap confidence intervals. The blue line shows a U^3 slope, where the proportionality constant (blue box) is calculated by taking the log-space mean of ε/U^3.
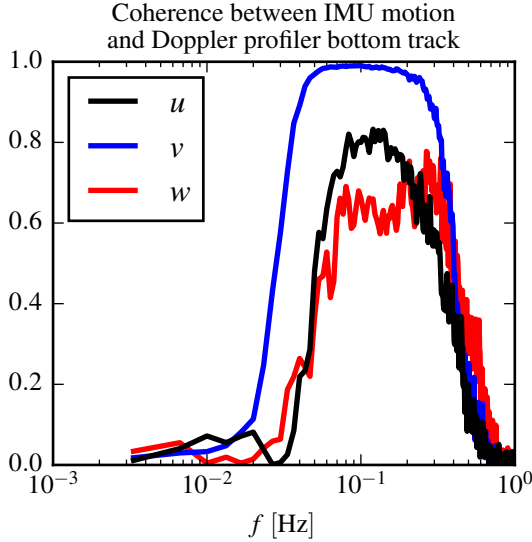
FIG. A1. Coherence between IMU-measured motion of StableMoor buoy and ADP bottom track velocity for $1.0 < \bar{U} < 1.5$. The vertical dotted line indicates the 95% confidence level for the 102 spectral windows in this estimate.

APPENDIX

A1. Comparing StableMoor $\vec{u}_{\mathrm{low}}$ to IMU $\vec{u}_{\mathrm{h}}$

In order to understand better understand the IMU's signal-to-noise ratio, it is instructive to compare the motion of the StableMoor buoy from the ADP bottom track measurements, u_{BT}, to the IMU's estimates of ADP motion. To do this, we compute the IMU's estimate of ADP motion using equation (2), and replacing ℓ^* with the vector that points from the IMU to the ADP head. We then linearly interpolated the ADP measurements onto the times of the ADV-IMU measurements.

The coherence between these two signals is high and statistically significant over 1.5 decades (from 0.03 to 0.8 Hz). The v component has the highest coherence, 98%, because this is the direction that has the most motion and therefore these estimates have a higher signal to noise ratio. The u and w components have slightly lower coherence, 80% and 65%, respectively, which indicates the *convolved* signal to noise ratio of these measurements.

On the low-frequency side, our interpretation is that the signal to noise ratio of the IMU increases dramatically below 0.03 Hz, resulting in low coherence. On the high-frequency side Doppler-noise in the ADP measurements contaminates its estimates of motion, causing the decrease in coherence at 0.8 Hz. A comparison of the phase between these signals shows that there is no lag between the measurements (not shown).

These results help to inform the selection of zero-lag filters used to estimate $\vec{u}_{\mathrm{low}}$ from u_{BT}. In particular, by

selecting 0.2 Hz, we target the middle of the coherence peak between the two measurements. Furthermore, the rapid decrease in coherence below 0.03 Hz provides an objective measure of the performance of the frequency at which IMU measured velocity becomes unreliable in the flow conditions we observed.

References

Afgan, I., J. McNaughton, S. Rolfo, D. Apsley, T. Stallard, and P. Stansby, 2013: Turbulent flow and loading on a tidal stream turbine by les and rans. *International Journal of Heat and Fluid Flow*, **43**, 96–108.

Alexander, S. R., and P. E. Hamlington, 2015: Analysis of turbulent bending moments in tidal current boundary layers. *Journal of Renewable and Sustainable Energy*, **7 (6)**, 063 118.

Alford, M. H., 2010: Sustained, full-water-column observations of internal waves and mixing near mendocino escarpment. *Journal of Physical Oceanography*, **40 (12)**, 2643–2660, doi:10.1175/2010JPO4502.1, URL http://dx.doi.org/10.1175/2010JPO4502.1, http://dx.doi.org/10.1175/2010JPO4502.1.

Bachmann, E. R., X. Yun, D. McKinney, R. B. McGhee, and M. J. Zyda, 2003: Design and implementation of MARG sensors for 3-DOF orientation measurement of rigid bodies. *International Conference on Robotics & Automation*, Taipei, Taiwan.

Barshan, B., and H. F. Durrant-Whyte, 1995: Inertial navigation systems for mobile robots. *IEEE Transactions on Robotics and Automation*, **11 (3)**, 328–342.

Bevly, D. M., 2004: Global positioning system (gps): A low-cost velocity sensor for correcting inertial sensor errors on ground vehicles. *Journal of dynamic systems, measurement, and control*, **126 (2)**, 255–264.

Cartwright, G. M., C. T. Friedrichs, P. J. Dickhudt, T. Gass, and F. H. Farmer, 2009: Using the acoustic doppler velocimeter (adv) in the mudbed real-time observing system. *Marine Technology for Our Future: Global and Local Challenges*.

Doherty, K., D. Frye, S. Liberatore, and J. Toole, 1999: A moored profiling instrument*. *Journal of Atmospheric and Oceanic Technology*, **16 (11)**, 1816–1829.

Egeland, M. N., 2014: Spectral evaluation of motion compensated ADV systems for ocean turbulence measurements. Ph.D. thesis, Florida Atlantic University.

Fer, I., and M. B. Paskyabi, 2014: Autonomous ocean turbulence measurements using shear probes on a moored instrument. *Journal of Atmospheric and Oceanic Technology*, **31 (2)**, 474–490, doi:10.1175/JTECH-D-13-00096.1, URL http://dx.doi.org/10.1175/JTECH-D-13-00096.1, http://dx.doi.org/10.1175/JTECH-D-13-00096.1.

Geyer, R. W., M. E. Scully, and D. K. Ralston, 2008: Quantifying vertical mixing in estuaries. *Environmental Fluid Mechanics*, **8**, 495–509, doi:10.1007/s10652-008-9107-2.

Goodman, L., E. R. Levine, and R. G. Lueck, 2006: On measuring the terms of the turbulent kinetic energy budget from an auv. *Journal of Atmospheric and Oceanic Technology*, **23 (7)**, 977–990, doi:10.1175/JTECH1889.1, URL http://dx.doi.org/10.1175/JTECH1889.1, http://dx.doi.org/10.1175/JTECH1889.1.

Grant, H. L., R. W. Stewart, and A. Moilliet, 1962: Turbulence spectra from a tidal channel. *Journal of Fluid Mechanics*, **12**, 241–263.

Gulmammadov, F., 2009: Analysis, modeling and compensation of bias drift in mems inertial sensors. *Recent Advances in Space Technologies, 2009. RAST'09. 4th International Conference on*, IEEE, 591–596.

Gunawan, B., V. S. Neary, and J. Colby, 2014: Tidal energy site resource assessment in the East River tidal strait, near Roosevelt Island, New York, NY (USA). *Renewable Energy*, **71**, 509–517, doi:10.1016/j.renene.2014.06.002.

Haid, M., and J. Breitenbach, 2004: Low cost inertial orientation tracking with kalman filter. *Applied Mathematics and Computation*, **153 (2)**, 567 – 575, doi:http://dx.doi.org/10.1016/S0096-3003(03)00656-8, URL http://www.sciencedirect.com/science/article/pii/S0096300303006568.

Hand, M. M., N. D. Kelley, and M. J. Balas, 2003: Identification of wind turbine response to turbulent inflow structures. Tech. Rep. NREL/CP-500-33465, National Renewable Energy Laboratory.

Harding, S., L. Kilcher, and J. Thomson, 2017: Turbulence measurements from compliant moorings - part 1: Motion characterization, in review.

Hayes, S., H. Milburn, and E. Ford, 1984: Tops: A free-fall velocity and ctd profiler. *Journal of Atmospheric and Oceanic Technology*, **1 (3)**, 220–236.

Kelley, N. D., B. J. Jonkman, G. N. Scott, J. T. Bialasiewicz, and L. S. Redmond, 2005: The impact of coherent turbulence on wind turbine aeroelastic response and its simulation. *WindPower*, Denver, Colorado, NREL/CP-500-38074, may 15-18.

Kilcher, L., J. Thomson, J. Talbert, and A. DeKlerk, 2016: Measuring turbulence from moored acoustic Doppler velocimeters: A manual to quantifying inflow at tidal energy sites. Tech. Rep. 62979, National Renewable Energy Laboratory. URL www.nrel.gov/docs/fy16osti/62979.pdf.

Kim, S. C., C. T. Friedrichs, J. P.-Y. Maa, and L. D. Wright, 2000: Estimating bottom stress in tidal boundary layer from acoustic doppler velocimeter data. *Journal of Hydraulic Engineering*, 399–406.

Kolmogorov, A. N., 1941: Dissipation of energy in the locally isotropic turbulence. *Dokl. Akad. Nauk SSSR*, **32 (1)**, 16–18, URL http://www.jstor.org/stable/51981.

Kraus, C., A. Lohrmann, and R. Cabrera, 1994: A new acoustic meter for measuring 3d laboratory flows. *Journal of Hydraulic Engineering*, **120**, 406–412.

Lohrmann, A., R. Cabrera, G. Gelfenbaum, and J. Haines, 1995: Direct measurements of reynolds stress with an acoustic doppler velocimeter. *Current Measurement, 1995., Proceedings of the IEEE Fifth Working Conference on*, 205–210, doi:10.1109/CCM.1995.516175.

Lorke, A., 2007: Boundary mixing in the thermocline of a large lake. *Journal of Geophysical Research: Oceans*, **112 (C9)**, n/a–n/a, doi:10.1029/2006JC004008, URL http://dx.doi.org/10.1029/2006JC004008, c09019.

Lueck, R. G., and D. Huang, 1999: Dissipation measurement with a moored instrument in a swift tidal channel. *Journal of atmospheric and oceanic technology*, **16**, 1499–1505.

Lumley, J., and E. Terray, 1983: Kinematics of turbulence convected by a random wave field. *Journal of Physical Oceanography*, **13 (11)**, 2000–2007.

Madgwick, S. O., A. J. Harrison, and R. Vaidyanathan, 2011: Estimation of imu and marg orientation using a gradient descent algorithm. *IEEE International Conference on Rehabilitation robotics*, IEEE.

McCaffrey, K., B. Fox-Kemper, P. E. Hamlington, and J. Thomson, 2015: Characterization of turbulence anisotropy, coherence, and intermittency at a prospective tidal energy site: Observational data analysis. *Renewable Energy*, **76**, 441–453.

McMillan, J. M., A. E. Hay, R. G. Lueck, and F. Wolk, 2016: Rates of dissipation of turbulent kinetic energy in a high reynolds number tidal channel. *Journal of Atmospheric and Oceanic Technology*, **33 (4)**, 817–837, doi:10.1175/JTECH-D-15-0167.1, URL http://dx.doi.org/10.1175/JTECH-D-15-0167.1, http://dx.doi.org/10.1175/JTECH-D-15-0167.1.

MicroStrain, I., 2010: Technical note: Coning and sculling. Tech. Rep. I0019, MicroStrain. URL http://files.microstrain.com/TN-I0019_3DM-GX3-25_Coning_And_Sculling.pdf.

MicroStrain, I., 2012: *3DM-GX3-15,-25 MIP Data Communications Protocol*. URL http://files.microstrain.com/3DM-GX3-15-25-MIP-Data-Communications-Protocol.pdf, retrieved January 2014.

Miller, S. D., T. S. Hristov, J. B. Edson, and C. A. Friehe, 2008: Platform motion effects on measurements of turbulence and air-sea exchange over the open ocean. *Journal of Atmospheric and Oceanic Technology*, **25 (9)**, 1683–1694, doi:10.1175/2008JTECHO547.1, URL http://dx.doi.org/10.1175/2008JTECHO547.1, http://dx.doi.org/10.1175/2008JTECHO547.1.

Morison, J. R., J. W. Johnson, and S. A. Schaaf, 1950: The force exerted by surface waves on piles. *Journal of Petroleum Technology*, **2 (05)**, 149–154.

Moum, J., and J. Nash, 2009: Mixing measurements on an equatorial ocean mooring. *Journal of Atmospheric and Oceanic Technology*, **26 (2)**, 317–336.

Mücke, T., D. Kleinhans, and J. Peinke, 2011: Atmospheric turbulence and its influence on the alternating loads on wind turbines. *Wind Energy*, **14**, 301–316.

Nash, J. D., L. F. Kilcher, and J. N. Moum, 2009: Structure and composition of a strongly stratified, tidally pulsed river plume. *Journal of Geophysical Research*, **114**, C00B12, doi:10.1029/2008JC005036.

Nash, J. D., E. Kunze, J. M. Toole, and R. W. Schmitt, 2004: Internal tide reflection and turbulent mixing on the continental slope. *Journal of Physical Oceanography*, **34 (5)**, 1117–1134, doi:10.1175/1520-0485(2004)034⟨1117:ITRATM⟩2.0.CO;2, URL http://dx.doi.org/10.1175/1520-0485(2004)034⟨1117:ITRATM⟩2.0.CO;2, http://dx.doi.org/10.1175/1520-0485(2004)034⟨1117:ITRATM⟩2.0.CO;2.

Nortek, 2005: *Vector Current Meter User Manual*. Vangkroken 2, NO-1351 RUD, Norway, h ed.

oáo Luis Marins, J., X. Yun, E. R. Bachmann, R. B. McGhee, and M. J. Zyda, 2001: An extended Kalman filter for quaternion-based orientation estimation using MARG sensors. *Internation cconference on intelligent robots and systems*.

Paskyabi, M. B., and I. Fer, 2013: Turbulence measurements in shallow water from a subsurface moored moving platform. *Energy Procedia*, **35**, 307 – 316, doi:http://dx.doi.org/10.1016/j.egypro.

2013.07.183, URL http://www.sciencedirect.com/science/article/pii/ S1876610213012691.

Rippeth, T. P., E. Williams, and J. H. Simpson, 2002: Reynolds stress and turbulent energy production in a tidal channel. *Journal of Physical Oceanography*, **32**, 1242–1251, doi:10.1175/1520-0485(2002) 032$\langle$1242:RSATEP$\rangle$2.0.CO;2.

Sreenivasan, K. R., 1995: On the universality of the Kolmogorov constant. *Physics of Fluids*, **7**, 2778–2784.

Stacey, M. T., S. G. Monismith, and J. R. Burau, 1999a: Measurements of reynolds stress profiles in unstratified tidal flow. *J. Geophys. Res.*, **104 (C5)**, 10 933–10 949, URL http://dx.doi.org/10.1029/ 1998JC900095.

Stacey, M. T., S. G. Monismith, and J. R. Burau, 1999b: Observations of turbulence in a partially stratified estuary. *Journal of Physical Oceanography*, **29**, 1950–1970.

Stahr, F. R., and T. B. Sanford, 1999: Transport and bottom boundary layerobservations of the north atlantic deep western boundary current at the blake outer ridge. *Deep Sea Research Part II: Topical Studies in Oceanography*, **46 (1)**, 205 – 243, doi:http://dx.doi.org/10. 1016/S0967-0645(98)00101-5, URL http://www.sciencedirect.com/ science/article/pii/S0967064598001015.

Thomson, J., B. Polagye, V. Durgesh, and M. Richmond, 2012: Measurements of turbulence at two tidal energy sites in Puget Sound, WA. *Journal of Oceanic Engineering*, **37 (3)**, 363–374, doi:10.1109/ JOE.2012.2191656.

Trowbridge, J. H., 1992: A simple description of the deepening and structure of a stably stratified flow driven by a surface stress. *Journal of Geophysical Research*, **97**, 15 529–15 543.

Trowbridge, J. H., W. R. Geyer, M. M. Bowen, and A. J. I. Williams, 1999: Near-bottom turbulence measurements in a partially mixed estuary: turbulent energy balance, velocity structure and along-channel momentum balance. *Journal of Physical Oceanography*, **29**, 3056–3072.

van der Walt, S., S. C. Colbert, and G. Varoquaux, 2011: The numpy array: A structure for efficient numerical computation. *Computing in Science & Engineering*, **13**, 22–30, doi:10.1109/MCSE. 2011.37, URL http://scitation.aip.org/content/aip/journal/cise/13/2/ 10.1109/MCSE.2011.37.

Voulgaris, G., and J. H. Trowbridge, 1998: Evaluation of the acoustic doppler velocimeter (adv) for turbulence measurements. *Journal of Atmospheric and Oceanic technology*, **15**, 272–289.

Walter, R. K., N. J. Nidzieko, and S. G. Monismith, 2011: Similarity scaling of turbulence spectra and cospectra in a shallow tidal flow. *Journal of Geophysical Research: Oceans*, **116 (C10)**.

Wiles, P. J., T. P. Rippeth, J. H. Simpson, and P. J. Hendricks, 2006: A novel technique for measuring the rate ot turbulent dissipation in the marine environment. *Geophysical Research Letters*, **33**, 21 608.

Winkel, D., M. Gregg, and T. Sanford, 1996: Resolving oceanic shear and velocity with the multi-scale profiler. *Journal of Atmospheric and Oceanic Technology*, **13 (5)**, 1046–1072.

Wyngaard, J. C., L. Rockwell, and C. A. Friehe, 1985: Errors in the measurement of turbulence upstream of an axisymmetric body. *Journal of Atmospheric and Oceanic Technology*, **2 (4)**, 605–614.

Zhang, Y., K. Streitlien, J. G. Bellingham, and A. B. Baggeroer, 2001: Acoustic doppler velocimeter flow measurement from an autonomous underwater vehicle with applications to deep ocean convection. *Journal of Atmospheric and Oceanic Technology*, **18 (12)**, 2038–2051, doi: 10.1175/1520-0426(2001)018$\langle$2038:ADVFMF$\rangle$2.0.CO;2, URL http://dx.doi.org/10.1175/1520-0426(2001)018$\langle$2038:ADVFMF$\rangle$ 2.0.CO;2, http://dx.doi.org/10.1175/1520-0426(2001)018$\langle$2038: ADVFMF$\rangle$2.0.CO;2.